

Numerical analysis of developing turbulent flow in a 180° bend tube by an algebraic Reynolds stress model

Hitoshi Sugiyama*[†] and Daisuke Hitomi

*Energy and Environmental Science, Graduate School of Engineering, Utsunomiya University,
7-1-2 Yoto, Utsunomiya 321-8585, Japan*

SUMMARY

A numerical analysis has been performed for three-dimensional developing turbulent flow in a 180° bend tube with straight inlet and outlet section used by an algebraic Reynolds stress model. To our knowledge, numerical investigations, which show the detailed comparison between calculated results and experimental data including distributions of Reynolds stresses, are few and far between. From this point of view, an algebraic Reynolds stress model in conjunction with boundary-fitted co-ordinate system is applied to a 180° bend tube in order to predict the anisotropic turbulent structure precisely. Calculated results are compared with the experimental data including distributions of Reynolds stresses. As a result of this analysis, it has been found that the calculated results show a comparatively good agreement with the experimental data of the time-averaged velocity and the secondary vectors in both the bent tube and straight outlet sections. For example, the location of the maximum streamwise velocity, which appears near the top or bottom wall in the bent tube, is predicted correctly by the present method. As for the comparison of Reynolds stresses, the present method has been found to simulate many characteristic features of streamwise normal stress and shear stresses in the bent tube qualitatively and has a tendency to under-predict its value quantitatively. Judging from the comparison between the calculated and the experimental results, the algebraic Reynolds stress model is applicable to the developing turbulent flow in a bent tube that is known as a flow with a strong convective effect. Copyright © 2005 John Wiley & Sons, Ltd.

KEY WORDS: numerical analysis; turbulent flow; algebraic Reynolds stress model; boundary fitted co-ordinate system; bent tube

1. INTRODUCTION

Since it has been recognized that the bend tube plays an important role as the machine element in many engineering fields, many researchers have presented the experimental and analytical results about the flow behaviour in the bent tube. In addition to this, bend tube flow

*Correspondence to: H. Sugiyama, Energy and Environmental Science, Graduate School of Engineering, Utsunomiya University, 7-1-2 Yoto, Utsunomiya 321-8585, Japan.

[†]E-mail: sugiyama@cc.utsunomiya-u.ac.jp

Received 22 January 2004

Revised 6 August 2004

Accepted 14 October 2004

is the basic flow as well as the near wall turbulence, separated flow, non-Newtonian flows, etc. However, when it is limited to turbulent flow of 180° bend with circular cross-section, very little has been reported. In this numerical analysis, special attention paid for developing turbulent flow of 180° bend with circular cross-section.

Rowe [1] has presented the experimental data for turbulent flow of 180° bend tube in the early stage. He had reported that the reversed flow of the secondary flow was generated locally near the bend angle 90° for the turbulent flow of 180° bend tube under the condition of Reynolds number 236 000. Azzola *et al.* [2] and Azzola and Humphrey [3] have measured the mean velocity and fluctuating velocities for turbulent flow of 180° bend tube in two flow conditions of Reynolds number, 57 400 and 110 000, by using laser-Doppler anemometer system. With regard to forced convection phenomenon of turbulent heat transfer, Baughn *et al.* [4] have measured comparatively in detail the temperature and Nusselt number distributions of 180° bend tube, which is the same bend tube presented by Azzola *et al.* [2]. Anwer *et al.* [5] have measured the streamwise velocity, secondary flow and six components of Reynolds stresses along the vertical and horizontal axes for 180° bend tube in Reynolds number 50 000 by hot wire anemometer. Their adopted bend tube has gently bent, that is, the curvature ratio between bend curvature radius and tube ratio is 12.89. The measurement has been carried out not only to the bend tube but also to the tangential straight tube and showed the developing behaviour of turbulent parameters. Adding to this, Anwer and So [6] have reported that the driving force of the secondary flow was classified into three kinds of forces, i.e. one is the centrifugal force, another is the imbalance between pressure gradient and centrifugal forces, which was dominant in the central region of the tube, and the other is anisotropic turbulence, which was active near the outer wall of the bend.

Contrasted with curvature ratio 12.89 of Anwer *et al.* [5], Sudou and Takami [7] have presented the experimental data for 180° bend tube with curvature ratio 4.0. They have measured the secondary flow and three components of Reynolds stresses at Reynolds number 60 000 by the hot wire technique. They have showed the contour maps of Reynolds stresses over the whole cross-section from the bend tube until the tangential straight tube in detail, while Anwer *et al.* [5] displayed local Reynolds stresses along vertical and horizontal axes. From the point of view for assessment of turbulent model, the experimental data of Sudou *et al.* are valuable results to evaluate the turbulent model, because they have measured developing turbulent flow of 180° bend tube in detail including distributions of Reynolds stresses.

As for the numerical calculation of turbulent flow for 180° bend tube, Azzola *et al.* [2] have predicted their experimental data [2, 3] by high Reynolds-number turbulence model, that is the so-called $k-\varepsilon$ model. Authors [8] have also calculated for the turbulent flow of 180° bend tube by low Reynolds-number turbulent model. In addition to this, authors [9] have predicted the experimental data measured by Baughn *et al.* [4] in forced convection of turbulent heat transfer in order to make the difference among the several kinds of two-equation models for temperature field clear. Sudou and Takami [10] and Aoyama *et al.* [11] have carried out numerical calculation using the transport equation of Reynolds stress and algebraic Reynolds stress model, respectively. Recently, numerical results of large eddy simulation have presented by Boerama and Nieuwstadt [12]. Although Lai *et al.* [13] have tried to predict the secondary flow driven through an-isotropic turbulence defined by Anwer and So [6] using the transport equation of Reynolds stress, they have not carried out the quantitative comparison with experimental data. In those numerical analyses, it may be said that many calculations have been performed for the fully developed turbulent flow and have

not been compared with the experimental data for the developing turbulent flow of the bent tube.

Considering from those references, the main object is to calculate for developing turbulent flow of 180° bend tube and to compare the calculated results quantitatively with the experimental data measured by Sudou and Takami [7] in detail, in which Reynolds stress results are involved. In this study, algebraic Reynolds stress model [14] is adopted in order to predict anisotropic turbulent flow precisely.

2. ANALYSIS

2.1. Numerical object and definition of co-ordinate system

Figure 1 shows the schematic diagram of the experimental apparatus of Sudou and Takami [7] and co-ordinate definitions of calculation. They have measured the developing turbulent flow of 180° bend with circular cross-section by the rotated hot wire technique, a method they themselves presented. The tubes of length 100D and 40D are attached to the inlet and outlet section of bend tube, respectively. The fully developed turbulent flow has been obtained by connecting 100D straight pipe in the entrance of the bent tube. In the experimental apparatus,

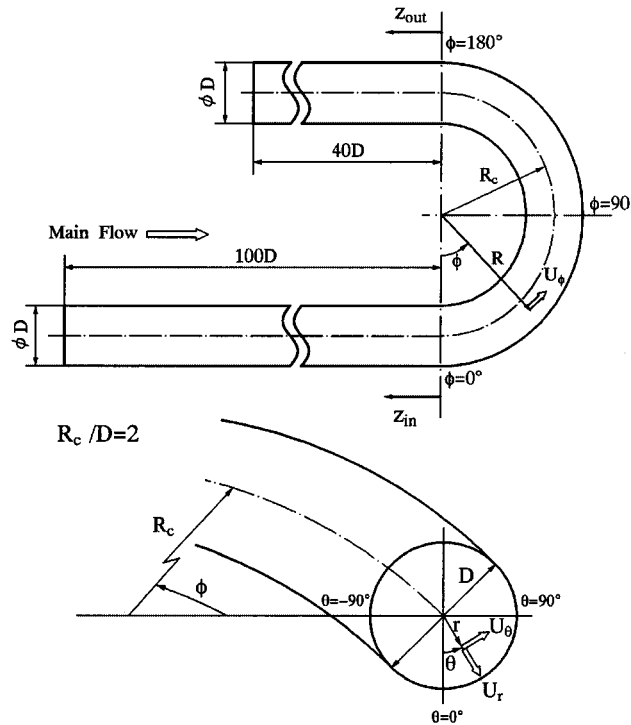


Figure 1. 180° bend tube and definition of co-ordinate system.

radius of curvature, diameter of tube D , the ratio of bend curvature radius for tube radius and Reynolds number are 208 mm, 104 mm, 4 and 60 000, respectively.

The co-ordinates of θ and r represent the bent tube angle along circumferential direction and radius direction in circular cross-section as shown in Figure 1. Symbols of Z_{in} and Z_{out} are the distance measured upstream from bend inlet section and distance measured downstream from bend outlet section, respectively. The arrow direction of Z_{in} and Z_{out} in Figure 1 is defined as the positive direction in this study.

2.2. The transport equation of Reynolds stresses

The anisotropy nature of the turbulence is expressed by the Reynolds stress equations. In order to deal with anisotropic turbulence, we have adopted the transport equation of Reynolds stress in numerical analysis. The exact formula of the transport equation of Reynolds stress is shown as follows.

$$\begin{aligned} \frac{D\overline{u_i u_j}}{Dt} = & - \left(\overline{u_i u_k} \frac{\partial U_j}{\partial X_k} + \overline{u_j u_k} \frac{\partial U_i}{\partial X_k} \right) + \frac{p}{\rho} \left(\frac{\partial u_i}{\partial X_j} + \frac{\partial u_j}{\partial X_i} \right) \\ & - \frac{\partial}{\partial X_k} \left\{ \overline{u_i u_j u_k} - \nu \frac{\partial \overline{u_i u_j}}{\partial X_k} + \frac{p}{\rho} (\delta_{jk} u_i + \delta_{ik} u_j) \right\} - 2\nu \frac{\partial \overline{u_i}}{\partial X_k} \frac{\partial \overline{u_j}}{\partial X_k} \end{aligned} \quad (1)$$

It is impossible to solve the above equation directly, so it is necessary to rewrite the several terms of Reynolds stress equation by introducing the turbulent model. Moreover, it is a fact from the point of numerical analysis that the convection term of the left-hand side and the diffusion term of the right-hand side are obstacles for getting numerical solution, because these terms are required to carry out iterative calculations in order to get the stable results. In this study, these terms are modelled by adopting Rodi's [15] approximation. As a result of this approximation, these two terms are transformed to an algebraic form from the differencing form. Therefore, the convection and diffusion terms in the above equation were modelled as follows:

$$\frac{D\overline{u_i u_j}}{Dt} - \text{Diff}_{ij} = \frac{\overline{u_i u_j}}{2k} (P_k - \varepsilon) \quad (2)$$

where Diff_{ij} corresponds to the third term on the right-hand side of Equation (1) and P_k represents the production term of turbulent energy equation.

A particularly problematic task here is the modelling of the pressure-strain correlation equation term, which is also defined as the redistribution term and is shown as the second term on the right-hand side of Equation (1). The pressure-strain term is composed of three parts, which are the interactions of the fluctuating velocities ($\pi_{ij,1} + \pi_{ji,1}$) and that of mean strain with the fluctuating velocities ($\pi_{ij,2} + \pi_{ji,2}$) and wall proximity effects ($\pi_{ij,w} + \pi_{ji,w}$). In the present calculation, we have adopted the Rotta's linear return to isotropy mode for ($\pi_{ij,1} + \pi_{ji,1}$) term, which term is shown in Table I.

Table I. Modelling of the pressure–strain correlation term.

$\pi_{ij,1} + \pi_{ji,1}$	$-C_1 \frac{\varepsilon}{k} \left(\overline{u_i u_j} - \frac{2}{3} k \delta_{ij} \right)$
$\pi_{ij,2} + \pi_{ji,2}$	$-\frac{C_2 + 8}{11} \left(P_{ij} - \frac{2}{3} P_k \delta_{ij} \right) + \zeta k \left(\frac{\partial U_i}{\partial x_j} + \frac{\partial U_j}{\partial x_i} \right)$ $-\frac{8C_2 - 2}{11} \left(D_{ij} - \frac{2}{3} P_k \delta_{ij} \right)$
$[\pi_{ij} + \pi_{ji}]_w$	$C_1 = C_1^* + C_1' f \left(\frac{L}{X_w} \right), \quad C_2 = C_2^* + C_2' f \left(\frac{L}{X_w} \right)$ $\zeta = \zeta^* + \zeta' f \left(\frac{L}{X_w} \right)$
$P_{ij} = \overline{u_i u_k} \frac{\partial U_j}{\partial x_k} - \overline{u_j u_k} \frac{\partial U_i}{\partial x_k}, \quad D_{ij} = \overline{u_i u_k} \frac{\partial U_k}{\partial x_j} - \overline{u_j u_k} \frac{\partial U_k}{\partial x_i}$	
$P_k = -\overline{u_k u_l} \frac{\partial U_k}{\partial x_l}, \quad f \left(\frac{L}{X_w} \right) = \frac{C_\mu^{3/4}}{\kappa} k^{3/2} \frac{1}{\varepsilon X_w}$	

For $\pi_{ij,2}$, the correlation is approximated in the form:

$$\pi_{ij,2} = \left(\frac{\partial U_l}{\partial X_m} \right) a_{lj}^{mi} \tag{3}$$

and a_{ij}^{mi} is the fourth-order tensor, which should satisfy the following kinematic constraints:

$$a_{ij}^{mi} = a_{ij}^{im} = a_{jl}^{im} \tag{4}$$

$$a_{li}^{mi} \frac{\partial U_l}{\partial X_m} = 0 \tag{5}$$

$$a_{jj}^{mi} = 2\overline{u_m u_i} \tag{6}$$

The above constraints arise from the symmetry condition, the mass conservation law and Green’s theorem, respectively. Although kinematic constraint of Equation (5) is different from the constraint presented by Launder *et al.* [16], we adopted Equation (5) because $\pi_{ij,2}$ is defined as the production between the fourth-order tensor and the mean strain as seen in Equation (3). Gessner and Eppich [17] have also presented these constraints and described in detail. The most general such tensor satisfying the symmetry constraints is written as

$$a_{ij}^{mi} = \alpha \delta_{lj} \overline{u_m u_i} + \beta (\delta_{ml} \overline{u_i u_j} + \delta_{mj} \overline{u_i u_l} + \delta_{il} \overline{u_m u_j} + \delta_{ij} \overline{u_m u_l})$$

$$+ c_2 \delta_{mi} \overline{u_l u_j} + \{ \eta \delta_{mi} \delta_{lj} + \nu (\delta_{ml} \delta_{ij} + \delta_{mj} \delta_{il}) \} k \tag{7}$$

which was presented by Launder *et al.* [16], where δ_{ij} represents Kronecker delta and c_2, α, β, η and ν are empirical constants.

In the case of Launder, Reece and Rodi, kinematic constraint $a_{ii}^{mi} = 0$ have been adopted instead of Equation (5). Therefore, we can get the following relation formula by using the fourth-order tensor of Equation (7):

$$a_{ii}^{mi} = (2\beta + \eta + 4\nu)\delta_{ml}k + (5\beta + \alpha + c_2)\overline{u_m u_l} \quad (8)$$

The corresponding equation in the present case is shown as follows:

$$a_{ii}^{mi} \frac{\partial U_l}{\partial X_m} = (2\beta + \eta + 4\nu)\delta_{ml}k \frac{\partial U_l}{\partial X_m} + (5\beta + \alpha + c_2)\overline{u_m u_l} \frac{\partial U_l}{\partial X_m} \quad (9)$$

In Equation (8), Launder *et al.* set constants of the first and second terms to be zero. However, the constant of the first term is not necessary at all times to be zero, because Kronecker delta satisfies zero when subscript m is not equivalent to subscript l . On the other hand, the first term of Equation (9) always shows zero whatever values m and l have. Therefore, the above inconsistency is avoided by introducing kinematic constraint of Equation (5). Besides, the constant of the second term only is set equal to zero in the present method.

Two constants α and β of Equation (7) are determined as a function of c_2 by adopting constraints of Equations (5) and (6). The influence of the mean strain ($\pi_{ij,2} + \pi_{ji,2}$) on the pressure–strain correlation is expressed by connecting Equation (3) with Equation (7) as shown in Table I. In Table I, $\zeta (= \eta + \nu)$ is an independent constant to be determined from experimental data and α and β are defined as the function of c_2 . In Launder, Reece and Rodi model, α , β , η and ν are defined as a function of only c_2 . Therefore, we can take into account more experimental data in the present model than Launder, Reece and Rodi model. As for modelling for mean strain rate ($\pi_{ij,2} + \pi_{ji,2}$), we have basically followed the same process presented by Launder *et al.* [16] except for adopting the constraint of Equation (5) for the fourth-order tensor.

The wall effect term ($\pi_{ij,w} + \pi_{ji,w}$) on turbulent stresses is modelled as shown in Table I by changing model constants. In Table I, $f(L/X_w)$ is a function that is related to the dimensionless distance from the wall and c_μ and κ represent the empirical constant and the von Karman constant, respectively. Function $f(L/X_w)$ takes unit near the wall and approaches zero with increasing the distance from the wall. The symbol X_w is the normal distance from the wall and L defines the length scale of turbulence. When $f(L/X_w)$ takes zero value, the model yields the correct Reynolds stress components for nearly homogeneous shear flow of Champagne *et al.* [18], while $f(L/X_w)$ is unit, magnitude of the stress components agree with consensus of near wall turbulence. Therefore, we have determined model constants by means of experimental data of near wall turbulence and homogeneous shear flows as mentioned above. Model constants used in this analysis are summarized in Table II.

Table II. Model constants of the pressure–strain correlation term.

C_1^*	C_2^*	ζ^*	C_1'	C_2'	ζ'	C_μ	κ
1.4	0.44	-0.16	-0.35	0.12	-0.1	0.09	0.42

The fourth term of Equation (1) is the homogeneous part of dissipation. The dissipation rate everywhere in the computed flow was assumed to be locally isotropic, i.e.

$$\varepsilon_{ij} = 2\nu \frac{\overline{\partial u_i}}{\partial X_k} \frac{\overline{\partial u_j}}{\partial X_k} = \frac{2}{3} \delta_{ij} \varepsilon \tag{10}$$

The transport equations of turbulent energy and dissipation are expressed as the following form:

$$\frac{Dk}{Dt} = \frac{\partial}{\partial X_j} \left\{ \left(\nu \delta_{jk} + c_s \frac{k}{\varepsilon} \overline{u_k u_j} \right) \frac{\partial k}{\partial X_k} \right\} - \overline{u_i u_k} \frac{\partial U_i}{\partial X_k} - \varepsilon \tag{11}$$

$$\frac{D\varepsilon}{Dt} = \frac{\partial}{\partial X_j} \left\{ \left(\nu \delta_{jk} + c_\varepsilon \frac{k}{\varepsilon} \overline{u_k u_j} \right) \frac{\partial \varepsilon}{\partial X_k} \right\} - \frac{\varepsilon}{k} \left(c_{1\varepsilon} \overline{u_i u_k} \frac{\partial U_i}{\partial X_k} + c_{2\varepsilon} \varepsilon \right) \tag{12}$$

Model constants c_s , c_ε , c_1 and c_2 , are 0.22, 0.18, 1.44 and 1.92, respectively.

2.3. *Boundary-fitted co-ordinate system*

It is required that the boundary condition is set along the shape precisely, when the shape complicatedly changes. Boundary-fitted co-ordinate system is the technique which transforms from the co-ordinate in the physical plane to that in the calculation plane. Numerical calculation is performed in the calculation plane. As the characteristic features of boundary-fitted co-ordinate system, it has been realized that it is easy to set boundary condition correctly along distorted shape, while governing equations are transformed to complicated equations from simple form equations in the physical plane.

The transformation from the physical plane to the calculation plane is carried out by the following mathematical theorem:

$$\frac{\partial}{\partial X_i} = \frac{\partial \xi}{\partial X_i} \frac{\partial}{\partial \xi} + \frac{\partial \eta}{\partial X_i} \frac{\partial}{\partial \eta} + \frac{\partial \zeta}{\partial X_i} \frac{\partial}{\partial \zeta} \tag{13}$$

The symbols ξ , ζ and η represent the co-ordinates of the calculation plane and are correspondent to streamwise direction, cross-sectional direction along calculation mesh in physical plane. For example, the momentum equation including the Reynolds stress is expressed as follows:

$$\frac{DU_i}{Dt} = -\frac{1}{\rho} \frac{\partial P}{\partial X_i} + \frac{\partial}{\partial X_j} \left(\nu \frac{\partial U_i}{\partial X_j} - \overline{u_i u_j} \right) \tag{14}$$

The Reynolds stress term in momentum equation is divided into two terms as in the following equation; i.e. one is the term containing the velocity gradient related with Reynolds stress and the other term is the remaining term except for the former term.

$$-\overline{u_i u_j} = \left(\frac{b}{a} \right)_{ij} \frac{\partial U_i}{\partial X_j} - \left(\frac{c}{a} \right)_{ij} \tag{15}$$

In the above equation, a and b denotes the coefficients of the Reynolds stresses and the velocity gradient, respectively, and c represents the remaining term except for these terms.

Here, we put

$$d_{ij} = v + \left(\frac{b}{a}\right)_{ij}, \quad e_{ij} = \left(\frac{c}{a}\right)_{ij} \quad (16)$$

so that the momentum equation can be rewritten in the following form:

$$\frac{\partial U_i}{\partial t} + \frac{\partial U_i U_j}{\partial X_j} = -\frac{1}{\rho} \frac{\partial P}{\partial X_i} + \frac{\partial}{\partial X_j} \left(d_{ij} \frac{\partial U_i}{\partial X_j} - e_{ij} \right) \quad (17)$$

Rewriting this formula by using the mathematical definition of Equation (13), we are able to obtain finally the transformed equation as follows:

$$\begin{aligned} & \frac{\partial U_i}{\partial t} + \frac{\partial}{\partial \xi} \left\{ \mathbf{U} U_i + \frac{P}{\rho} \frac{\partial \xi}{\partial X_i} - l_1 \frac{\partial U_i}{\partial \xi} - l_2 \frac{\partial U_i}{\partial \eta} - l_3 \frac{\partial U_i}{\partial \zeta} + e_{i3} \frac{\partial \xi}{\partial X_3} + e_{i2} \frac{\partial \xi}{\partial X_2} + e_{i1} \frac{\partial \xi}{\partial X_1} \right\} \\ & + \frac{\partial}{\partial \eta} \left\{ \mathbf{V} U_i + \frac{P}{\rho} \frac{\partial \eta}{\partial X_i} - l_2 \frac{\partial U_i}{\partial \xi} - l_4 \frac{\partial U_i}{\partial \eta} - l_5 \frac{\partial U_i}{\partial \zeta} + e_{i3} \frac{\partial \eta}{\partial X_3} + e_{i2} \frac{\partial \eta}{\partial X_2} + e_{i1} \frac{\partial \eta}{\partial X_1} \right\} \\ & + \frac{\partial}{\partial \zeta} \left\{ \mathbf{W} U_i + \frac{P}{\rho} \frac{\partial \zeta}{\partial X_i} - l_3 \frac{\partial U_i}{\partial \xi} - l_5 \frac{\partial U_i}{\partial \eta} - l_6 \frac{\partial U_i}{\partial \zeta} + e_{i3} \frac{\partial \zeta}{\partial X_3} + e_{i2} \frac{\partial \zeta}{\partial X_2} + e_{i1} \frac{\partial \zeta}{\partial X_1} \right\} \quad (18) \end{aligned}$$

$$\begin{aligned} \mathbf{U} &= U_1 \frac{\partial \xi}{\partial X_1} + U_2 \frac{\partial \xi}{\partial X_2} + U_3 \frac{\partial \xi}{\partial X_3} \\ \mathbf{V} &= U_1 \frac{\partial \eta}{\partial X_1} + U_2 \frac{\partial \eta}{\partial X_2} + U_3 \frac{\partial \eta}{\partial X_3} \\ \mathbf{W} &= U_1 \frac{\partial \zeta}{\partial X_1} + U_2 \frac{\partial \zeta}{\partial X_2} + U_3 \frac{\partial \zeta}{\partial X_3} \end{aligned} \quad (19)$$

In the above equation, \mathbf{U} , \mathbf{V} and \mathbf{W} are components of the contravariant velocity. The symbol l_i represents the metric tensor appearing as a result of transformation. Contravariant velocity and metric tensor are defined as following forms.

$$\begin{aligned} l_1 &= d_{i3} \frac{\partial^2 \xi}{\partial X_3^2} + d_{i2} \frac{\partial^2 \xi}{\partial X_2^2} + d_{i1} \frac{\partial^2 \xi}{\partial X_1^2}, \quad l_2 = d_{i3} \frac{\partial \xi}{\partial X_3} \frac{\partial \eta}{\partial X_3} + d_{i2} \frac{\partial \xi}{\partial X_2} \frac{\partial \eta}{\partial X_2} + d_{i1} \frac{\partial \xi}{\partial X_1} \frac{\partial \eta}{\partial X_1} \\ l_3 &= d_{i3} \frac{\partial \xi}{\partial X_3} \frac{\partial \zeta}{\partial X_3} + d_{i2} \frac{\partial \xi}{\partial X_2} \frac{\partial \zeta}{\partial X_2} + d_{i1} \frac{\partial \xi}{\partial X_1} \frac{\partial \zeta}{\partial X_1}, \quad l_4 = d_{i3} \frac{\partial^2 \eta}{\partial X_3^2} + d_{i2} \frac{\partial^2 \eta}{\partial X_2^2} + d_{i1} \frac{\partial^2 \eta}{\partial X_1^2} \\ l_5 &= d_{i3} \frac{\partial \eta}{\partial X_3} \frac{\partial \zeta}{\partial X_3} + d_{i2} \frac{\partial \eta}{\partial X_2} \frac{\partial \zeta}{\partial X_2} + d_{i1} \frac{\partial \eta}{\partial X_1} \frac{\partial \zeta}{\partial X_1}, \quad l_6 = d_{i3} \frac{\partial^2 \zeta}{\partial X_3^2} + d_{i2} \frac{\partial^2 \zeta}{\partial X_2^2} + d_{i1} \frac{\partial^2 \zeta}{\partial X_1^2} \end{aligned} \quad (20)$$

The other governing equations also are able to transform from the physical plane to the calculation plane following the above procedure.

2.4. Numerical analysis

Considering the symmetry of the circular cross-section, we set the calculated region to half of the circular cross-section. Although the inlet length of the straight tube in experimental apparatus is $100D$ in order to obtain the fully developed turbulent flow, the inlet length of straight tube in the calculation is set up $40D$ to save computational time. The length of the outlet straight tube is also set up $40D$, which is the same length for the experimental apparatus. Since the present model can be classified into the high Reynolds-number turbulent model, wall function method is adopted as the boundary condition for turbulent energy and dissipation. The inflow condition of turbulent energy and dissipation were assumed to be $k = U_{b2} \times 10^{-5}$ and $\varepsilon = k^{3/2}/D$, respectively, because the inlet condition of turbulent energy and dissipation were uncertain even in the experiment. The outlet boundary conditions set the Neumann condition. The governing equations were discretized by the differencing scheme and QUICK (third-order up-wind differencing scheme) was used for discretion of convection term. The Reynolds number is the same as that of the experiment that is 60 000, based on mean velocity and diameter. The calculation grids are located 41×21 in the half region of total cross-section and 140 along the main flow direction. Therefore, the total amount of calculation grids are 120 540. Figure 2 shows the grid layouts for calculation, i.e. one is calculation grid for symmetrical plane ($\pm 90^\circ$ plane) and the other is that for half region of circular cross-section.

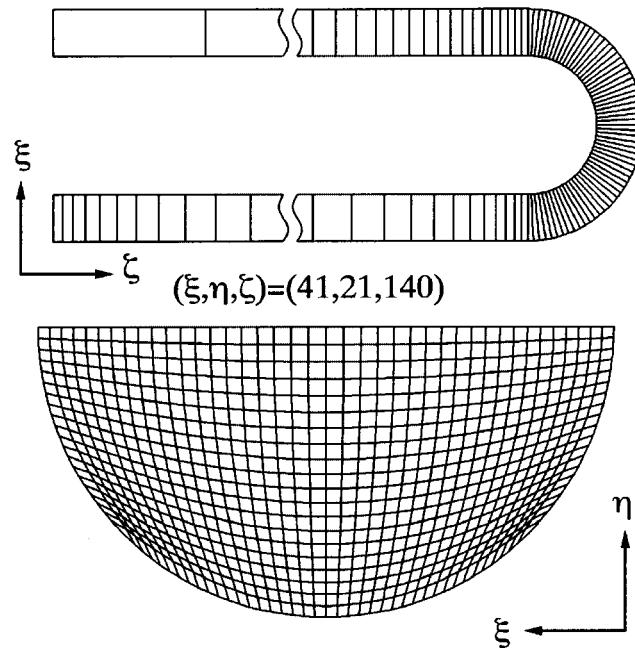


Figure 2. Computational mesh layout.

3. RESULTS AND DISCUSSIONS

3.1. Comparison of mean velocity

The calculated results of streamwise mean velocities are compared with the experimental data for the bent tube and tangential straight tube in Figure 3. The values were made dimensionless by bulk velocity. The left- and the right-hand sides of circular cross-section are correspondent to the inner and outer walls for the bent tube, respectively. It is pointed out as the characteristic feature in both results that the maximum mainstream velocity is produced at the inner wall side at the bent inlet $\phi = 0^\circ$ and curved station $\phi = 30^\circ$. Such a phenomenon is a remarkable feature especially for the flow with the sharp bending tube. At station $\phi = 60^\circ$ in both results, there are distorted contour lines which protruded from the inner wall towards the central region of the bent tube. These distorted contour lines suggest that low-velocity fluid near the wall is conveyed to the inner wall side by the secondary flow. Such a tendency of flow behaviour is

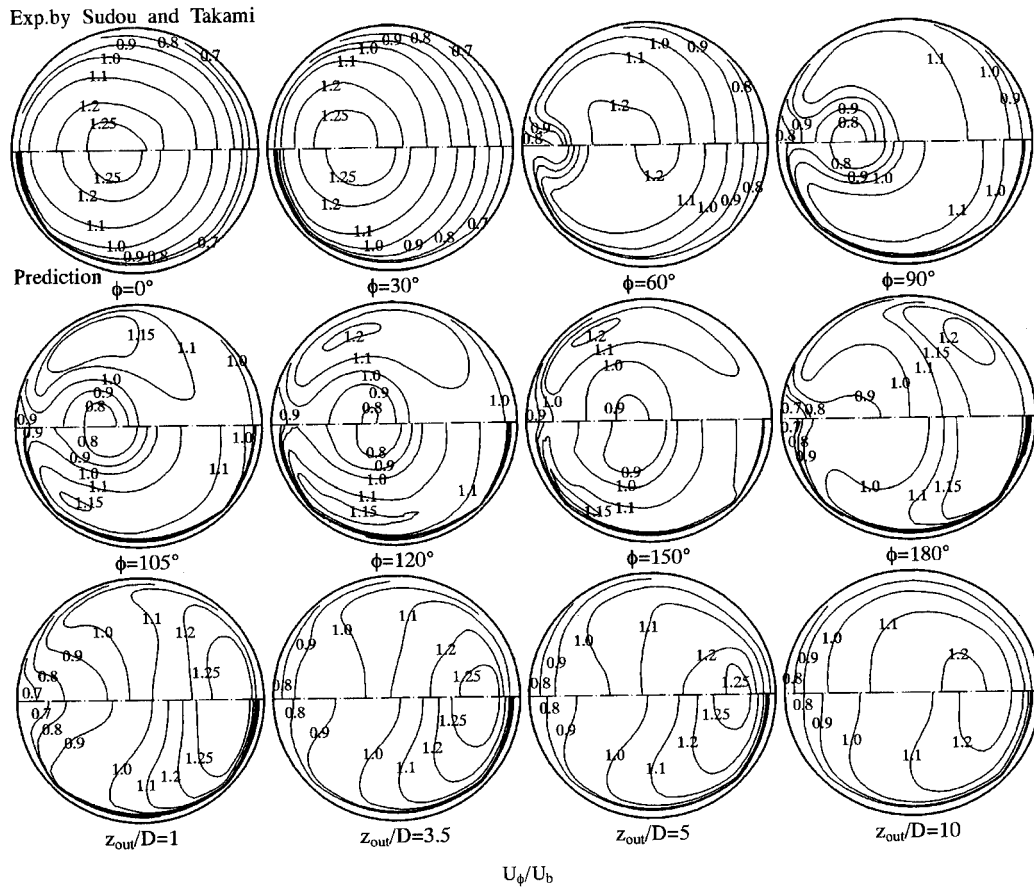


Figure 3. Comparison of streamwise mean velocity.

specially recognized in station $\phi = 90^\circ$. Besides, both the calculated and experimental results of $\phi = 105, 120, 150^\circ$ show that low-velocity fluid is transferred to the central region by the secondary flow as the flow develops. At station $\phi = 180^\circ$ of experimental data, the region of low-velocity fluid is generated again near the inner wall of the bent tube. The presented method is also able to reproduce this characteristic feature reasonably. In the outlet straight tube, the contour lines approach gradually the concentric circular contour distributions of fully developed turbulent flow downstream, continuously forming the high value of contours near the outer wall side of the circular tube. The numerical calculation has predicted not only qualitative but also quantitatively these characteristic phenomena. Moreover, comparison of the calculated results with the experimental data at $\phi = 105, 120, 150, 180^\circ$ shows that numerical calculation has reproduced the maximum streamwise velocity in the vicinity of the bottom wall as well as the experimental data except for the station $\phi = 180^\circ$. Considering the maximum streamwise velocity is not observed near the wall for the turbulent flow of 90° bend tube [19], such generation of maximum streamwise velocity in the vicinity of the wall may be a peculiar phenomenon for 180° bend tube. This phenomenon is caused by forming the low-velocity fluid in the central region induced by the secondary flow.

Both numerical and experimental results of the contour lines of streamwise velocity on the symmetrical plane ($\theta = \pm 90^\circ$) for the top and bottom walls are shown in Figure 4. The regions of low-velocity fluid are recognized near the inner wall between $\phi = 30$ and 60° and the inner wall of the outlet straight tube in both results. The calculation has estimated the experimental value comparatively well. There is the strong correlation between contour distributions and secondary flow derived by the pressure gradient.

Figure 5 shows the comparison of the calculated secondary flow with the measured secondary flow. At the inlet station of the bent tube $\phi = 0^\circ$ in both results, the secondary flow has been formed uniformly from the outer wall towards the inner wall as a result of generating high pressure gradient near the outer wall of the bent tube. From both the results of station $\phi = 30^\circ$, secondary flow moves from the inner wall to outer wall along the symmetric plane and the paired vortex is formed covering the total cross-section. The strength of secondary flow increases gradually with the development of the flow, and the low-velocity fluid is carried to the inner wall side. The contour lines of the inner wall will be greatly distorted by transporting low-velocity fluid. But after the flow passes at station $\phi = 90^\circ$, it is clear from both results that the strength of secondary flow attenuates conversely. It can be also pointed out as the common phenomenon of both results that the strength of secondary flow rapidly decreases in the downstream straight tube section. Although Lai *et al.* [13] has estimated the existence of secondary flow of the second kind generated by anisotropic turbulence in the vicinity outer wall, both results do not indicate such a secondary flow of the second kind in this sharp bent tube.

Figure 6 displays a comparison of the wall static pressure along the streamwise flow at the location of $\theta = \pm 90, \pm 45$ and 0° . Both results show that negative pressure gradient is formed at the outer wall near the bend inlet; on the other hand, the positive pressure gradient is generated at the inner wall near the bend inlet. At the bend inlet, secondary flow generated from the outer wall to the inner wall is produced by the pressure difference between the outer and inner walls. When special attention is paid for pressure coefficient along the inner wall ($\theta = -90^\circ$), it is found out as a characteristic feature that the pressure coefficient increases until station $\phi = 75^\circ$ and decreases monotonically after passing $\phi = 75^\circ$. The calculation has also quantitatively predicted this remarkable phenomenon. This pressure coefficient rise along inner

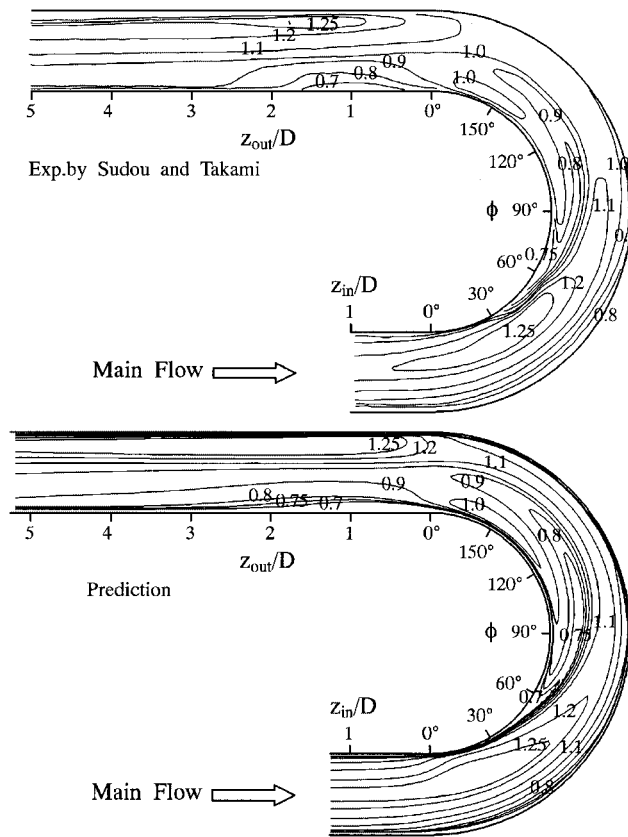


Figure 4. Comparison of streamwise mean velocity on $\pm 90^\circ$ plane.

wall may be produced by the existence of the outer wall located after station 90° , which wall acts as resistance for the flow near the inner wall placed before station 90° .

3.2. Comparison of Reynolds stresses

Comparisons of streamwise velocity fluctuation are shown in Figure 7. The contour lines of bent inlet $\phi = 0^\circ$ show asymmetric pattern with respect to vertical axis to move slightly to the inner wall side in both results. In the experimental contours, the strong intensity of velocity fluctuation is generated near the inner wall side and velocity fluctuation increases gradually until it reaches the maximum value with 18% of bulk velocity at station $\phi = 105^\circ$. Although the calculation has not predicted precisely the maximum value of velocity fluctuation, the calculation has been able to reproduce the characteristic phenomenon without large discrepancy. The strong intensity of velocity fluctuation is also generated near the region of the inner wall between the bent outlet and $Z_{out}/D = 1$ of the straight tube in both results. It is understood from both results at $Z_{out}/D = 10$ of straight tube that the long length of tube is needed to obtain the fully developed turbulent flow after the flow passing the bent tube.

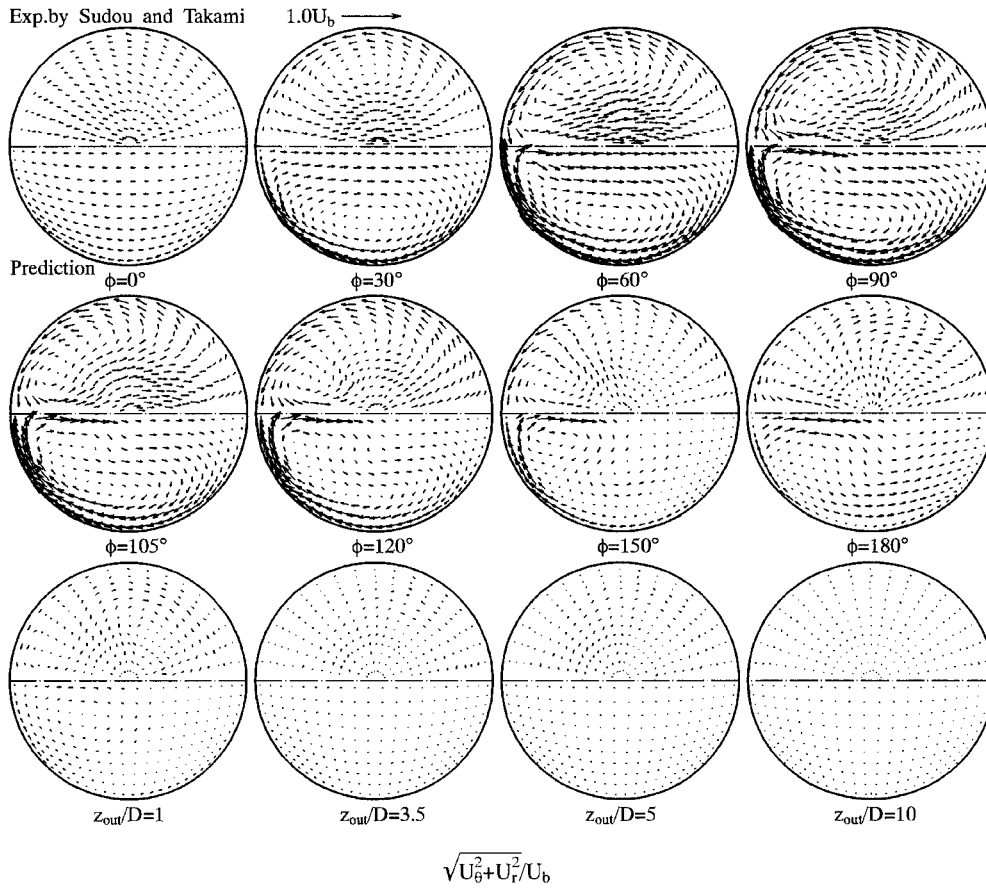


Figure 5. Comparison of secondary flow.

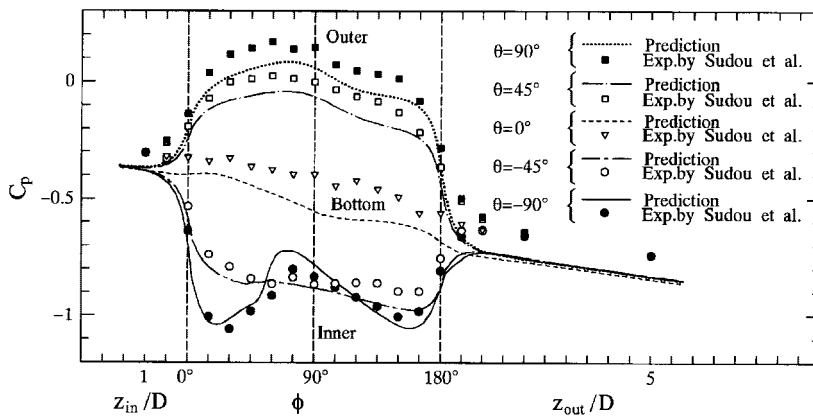


Figure 6. Comparison of secondary flow.

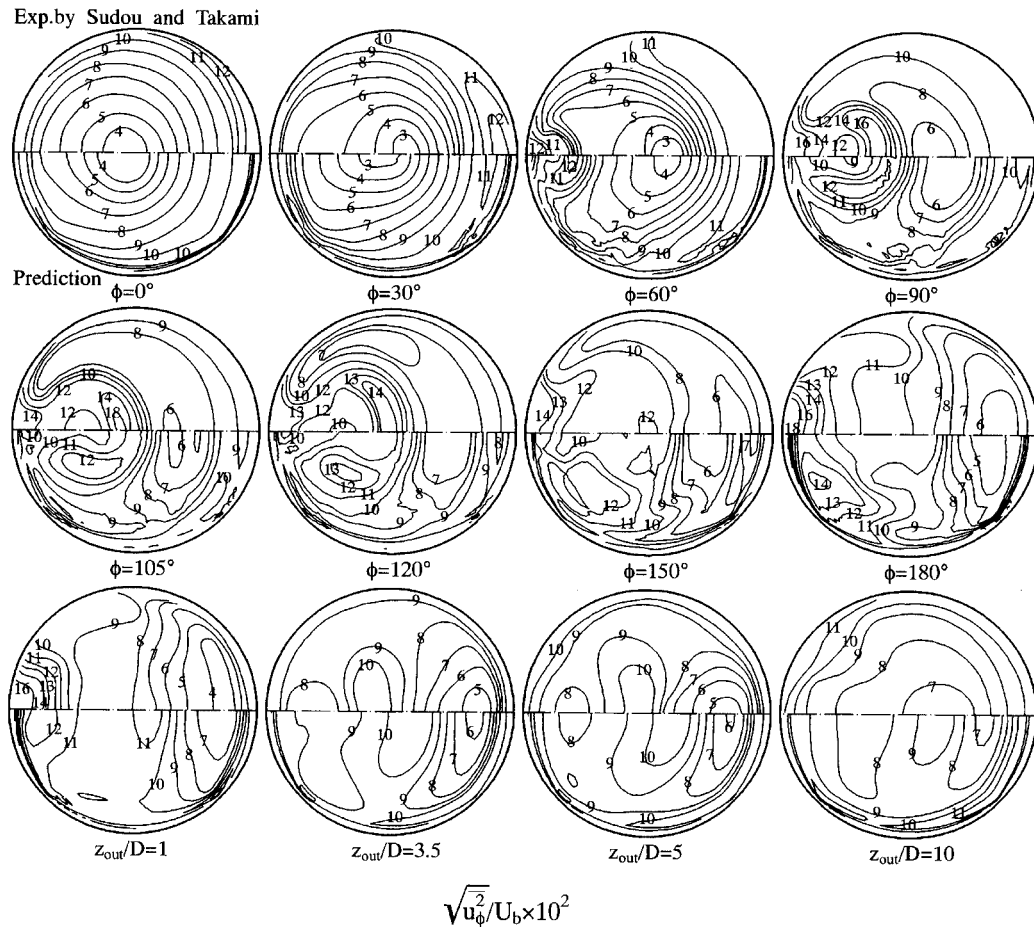


Figure 7. Comparison of streamwise velocity fluctuation.

Figures 8 and 9 show the comparison of shear stresses $\overline{u_\phi u_r}$ and $\overline{u_\phi u_\theta}$, respectively. From the experimental data, it is observed as a distinctive feature that the concentric circular contour lines with positive sign at the bent inlet gradually changes its profile of distribution with increasing negative sign region as the flow develops and the absolute maximum value of shear stress is produced above the symmetry axis. Besides, the contour line with zero value has the shape of the circular distribution in the outlet straight tube, which is greatly different from the contour lines in the bent tube. The calculation has also reproduced such characteristic phenomenon mentioned above. As for the shear stress $\overline{u_\phi u_\theta}$, relative high value of shear stress is generated near the upper and bottom walls as shown in the results of $\phi = 0$ and 30° and the region with the opposite sign is formed by generating zero lines after the flow passing $\phi = 60^\circ$. The calculation has predicted the region with the opposite sign up to $\phi = 150^\circ$ comparatively well, but the distribution of the outlet section $\phi = 180^\circ$ is slightly different

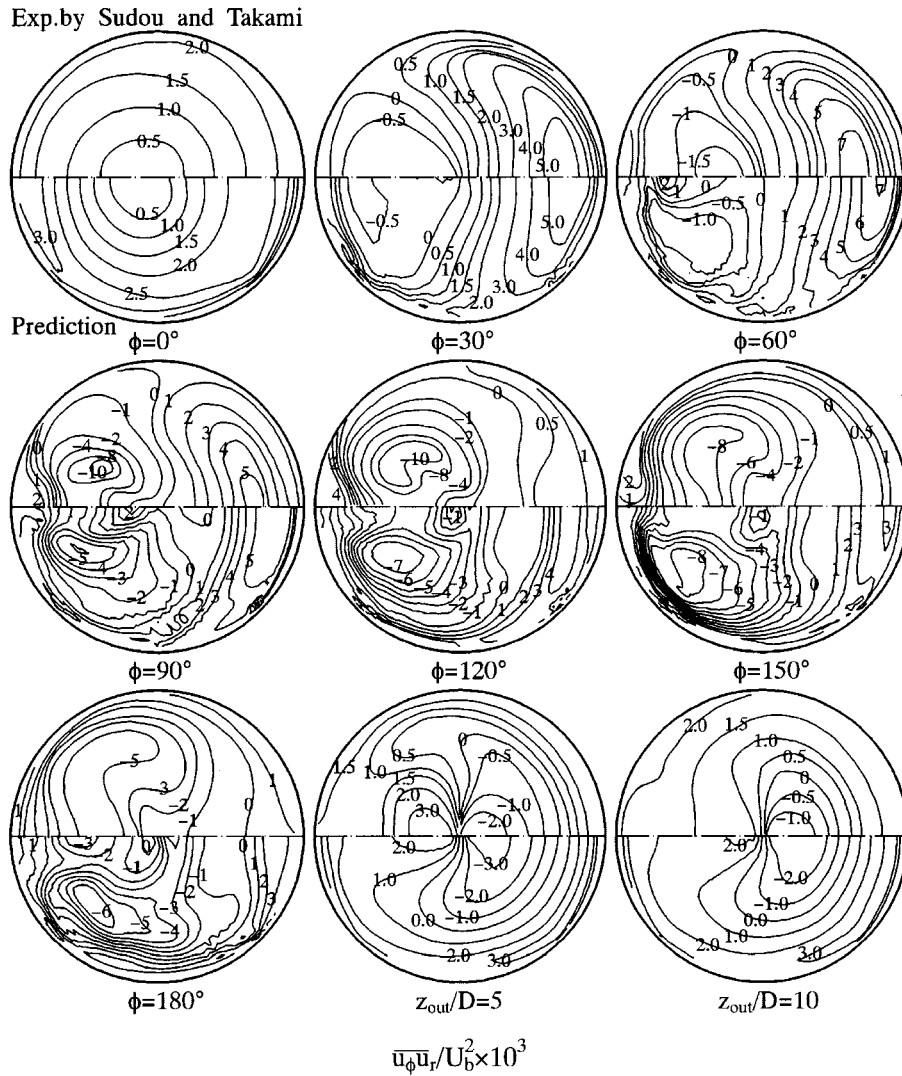


Figure 8. Comparison of shear stress $\overline{u_\phi u_r}$.

from the experimental result. Downstream of the straight tube, it is understood from both the results that almost all regions of the cross-section are occupied by the negative value of shear stress. The comparison results described above suggest that the algebraic Reynolds stress model is able to predict the developing turbulent flow of the bent tube that is characterized as complicated turbulent flow.

3.3. Comparison of averaged values over the cross-section

Figure 10 shows comparison of the biased length \bar{x}/D that is defined as the shortest distance between the vertical axis and the gravity point of streamwise velocity over the half cross-

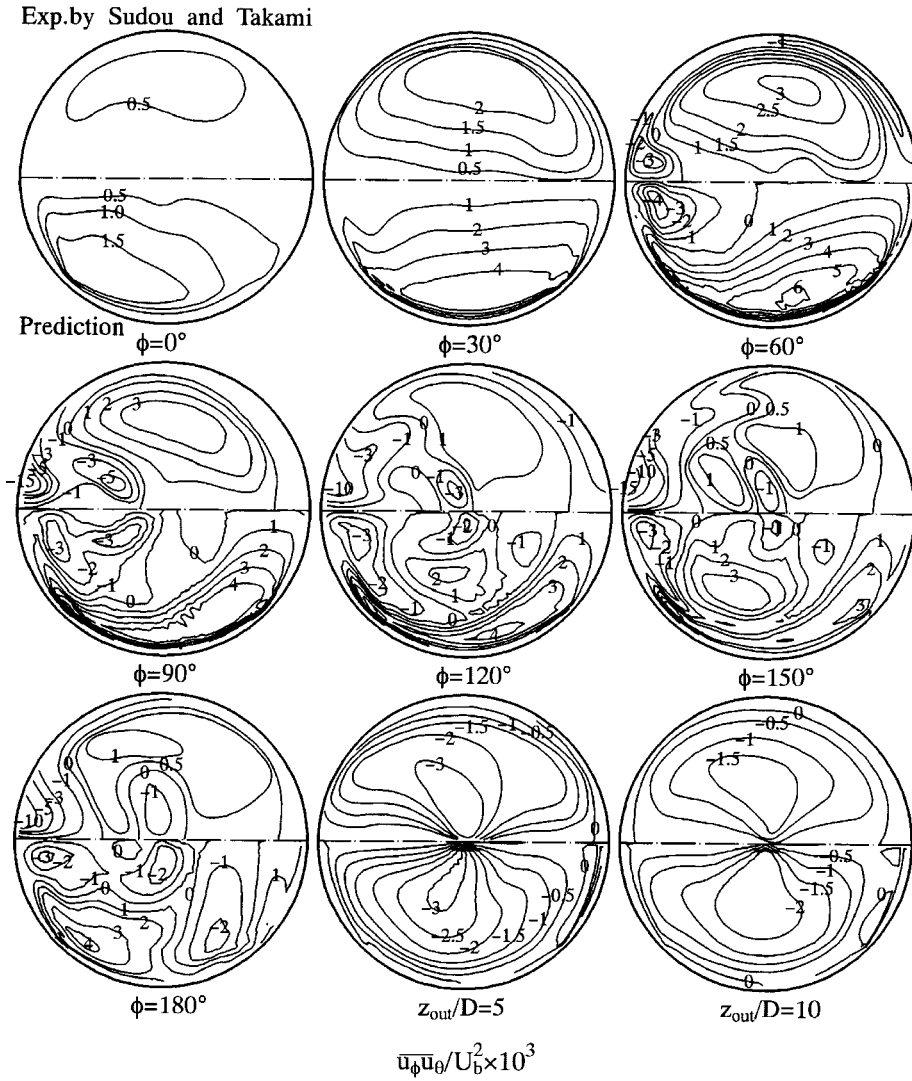


Figure 9. Comparison of shear stress $\bar{u}_\phi \bar{u}_\theta$.

section, the averaged strength of secondary I_s and averaged strength of turbulent energy I_k over the half cross-section. Values for these parameters are estimated by the following equations.

$$\frac{\bar{x}}{D} = \frac{8}{\pi D^2 U_b} \int_{-\pi/2}^{\pi/2} \int_0^{D/2} \frac{r \sin \theta}{D} U_\phi r dr d\theta \quad (21)$$

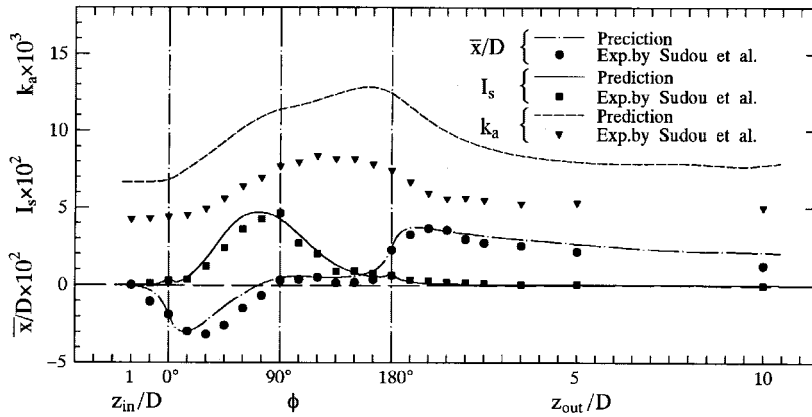


Figure 10. Comparison of mean values of I_k , I_s and \bar{x}/D .

$$I_s = \frac{8}{\pi D^2 U_b} \int_{-\pi/2}^{\pi/2} \int_0^{D/2} (U_\phi^2 + U_r^2) r \, dr \, d\theta \tag{22}$$

$$I_k = \frac{8}{\pi D^2 U_b} \int_{-\pi/2}^{\pi/2} \int_0^{D/2} \frac{1}{2} (\overline{u_\phi^2} + \overline{u_\theta^2} + \overline{u_r^2}) r \, dr \, d\theta \tag{23}$$

From the experimental result, it has been found out that, after the gravity point of streamwise velocity moves to the inner wall near the inlet section of the bent tube, its gravity point approaches gradually to the vertical axis and rapidly moves to the outer wall side near the outlet section of the bent tube as the flow develops. The maximum value of the biased length is generated in the downstream straight tube. The calculated result of \bar{x}/D is in good agreement with the experimental results. Besides, it is proven from comparison of both results that the averaged strength of secondary flow takes the maximum value near the $\phi = 90^\circ$. Contrary to this, the calculation over-predicts the averaged strength of turbulent energy of the experimental data.

4. CONCLUSIONS

A numerical analysis has been performed for three-dimensional developing turbulent flow in a 180° bend tube with straight inlet and outlet sections using by an algebraic Reynolds stress model and boundary-fitted co-ordinate system. Calculated results are compared with the experimental data measured by Sudou and Takami [7] to confirm the validity of the present method. As results of this analysis, the following conclusions are summarized:

- (1) The present method is able to predict quantitatively and qualitatively the experimental feature, i.e. the location of maximum streamwise velocity formed in the vicinity of circumference wall after passing the region where low velocity is generated near the inner wall side of inlet plane of the bent tube.

- (2) Calculated developing behaviour of the secondary flow is in good agreement with the experimental results.
- (3) On the results of streamwise velocity fluctuation, although the present method tends to estimate its value as small, the present method predicts well the region with high value generated near the inner wall, which recognizes after $\phi = 60^\circ$ and distributions of streamwise velocity fluctuation in the downstream straight tube.
- (4) It has been found from the experimental results that the distributions of shear stress $\overline{u_\phi u_r}$ for the bent tube show the negative region in the inner wall side and the positive region in the outer wall side, which are separated by contour line with zero value. For the downstream straight tube, its distributions of shear stress display the negative region in the central part and the positive region in the circumference wall by forming zero line. The present method also predicts well these characteristic features of experiments.
- (5) The calculated results of shear stress $\overline{u_\phi u_\theta}$ coincide with the experiment, i.e. the relative high value of shear stress is generated near the upper and bottom walls and the region with the opposite sign is formed by generating zero lines after the flow passing $\phi = 60^\circ$.
- (6) In view of the results for comparison with experimental data, it must be said that the presented algebraic Reynolds stress model is applicable to predict reasonably the developing turbulent flow of the bent tube.

NOMENCLATURE

C_p	pressure coefficient $2(P - P_{\text{ref}})/\rho U_b^2$
D	diameter of circular tube
k	turbulent energy
P	pressure
P_{ref}	pressure at $Z_{\text{in}}/D = 17.6$
Re	Reynolds number $U_b D/\nu$
R	radius direction of tube
r	radius direction of tube
R_c	radius of curvature
U_ϕ, U_θ, U_r	mean velocity along co-ordinates of ϕ, θ, r directions
u_ϕ, u_θ, u_r	fluctuating velocity along co-ordinates of ϕ, θ, r directions
U_b	bulk velocity
$\overline{u_i u_j}$	Reynolds stresses
Z	co-ordinate along the straight tube
ε	turbulent dissipation
ν	kinematics viscosity
ϕ	bent tube angle
θ	circumferential direction of circular cross-section

REFERENCES

1. Rowe M. Measurements and computations flow in pipe bends. *Journal of Fluid Mechanics* 1970; **43**:771–783.
2. Azzola J, Humphrey JAC, Iacovides H, Launder BE. Developing turbulent flow in a U-bend of circular cross-section: measurement and computation. *Transactions of the ASME, Journal of Fluid Engineering* 1986; **108**: 214–221.

3. Azzola J, Humphrey JAC. Developing turbulent flow in a 180° curved pipe and its downstream tangent. *Report LBL-17681*. Lawrence Berkeley Laboratory, University of California, 1984.
4. Baughn JW, Iacovides H, Jackson DC, Launder BE. Local heat transfer measurements in turbulent flow around a 180° pipe bend. *Transactions of the ASME, Journal of Heat Transfer* 1987; **109**:43–48.
5. Anwer M, So RMC, Lai G. Perturbation by and recovery from bend curvature of a fully developed turbulent pipe flow. *Physics of Fluids Series A* 1989; **1–8**:1387–1397.
6. Anwer M, So RMC. Swirling turbulent flow through a curved pipe. *Experiments in Fluids* 1993; **14**:85–96.
7. Sudou K, Takami T. Turbulent flow of 180° bend with circular cross section. *Turbo Machinery* 1992; **20–12**: 33–38 (in Japanese).
8. Sugiyama H, Akiyama M, Kikuchi Y. Numerical analysis of three-dimensional turbulent flow in 180°-bent tube by low-Reynolds-number turbulent models. *Transactions of the JSME* 1995; **61–585**:1707–1713 (in Japanese).
9. Sugiyama H, Akiyama M, Shimizu T. Numerical analysis of three-dimensional turbulent heat transfer in a 180°-bent tube by tow-equation heat transfer models. *Transactions of the JSME* 1996; **62–596**:1530–1537 (in Japanese).
10. Sudou K, Takami T. Numerical analysis of turbulent flow in a curved circular pipe by a Reynolds stress model. *Transactions of the JSME* 1988; **54–506**:2755–2761 (in Japanese).
11. Aoyama Y, Hijikata K, Futakami K. Numerical analysis of turbulent flow in a curved tube by a combination of the $k-\varepsilon$ model and the algebraic turbulent stress model. *Transactions of the JSME* 1990; **56–528**:2300–2308 (in Japanese).
12. Boerama BJ, Nieuwstadt FTM. Large-eddy simulation of turbulent flow in a curved pipe. *Transactions of the ASME, Journal of Fluid Engineering* 1996; **118**:248–258.
13. Lai YG, So RMC, Zhang HS. Turbulence-driven secondary flows in a curved pipe. *Theoretical and Computational Fluid Dynamics* 1991; **3**:163–180.
14. Sugiyama H, Akiyama M, Matsumoto M. Numerical analysis of fully developed turbulent flow in a square duct with two roughened walls. *Computational Fluid Dynamics Journal* 1993; **2–3**:319–338.
15. Rodi W. A new algebraic relation for calculating the Reynolds stresses. *Zeitschrift für Angewandte Mathematik und Mechanik* 1976; **56**:219–221.
16. Launder BE, Reece GJ, Rodi W. Progress in the development of a Reynolds stress turbulent closure. *Journal of Fluid Mechanics* 1975; **22**:537–566.
17. Gessner FB, Eppich HM. A near-wall pressure-strain model for turbulent corner flows. *Proceedings of the 3rd Symposium on Turbulent Shear Flows* 1981; 25–32.
18. Champagne FH, Harris VG, Corrisn S. Experimental on nearly homogeneous turbulent shear flow. *Journal of Fluid Mechanics* 1970; **41**:81–139.
19. Sudou K, Takami T, Yano K. Turbulent flow in a circular-sectioned 90° bend. *Transactions of the JSME* 1992; **58–548**:1015–1021 (in Japanese).